第 49 卷第 3 期　　硅　酸　盐　学　报　　Vol. 49，No. 3
2021 年 3 月　　JOURNAL OF THE CHINESE CERAMIC SOCIETY　　March，2021
http://www.gxyb.cbpt.cnki.net　　**DOI**：10.14062/j.issn.0454-5648.20200538

A/*B* 位离子掺杂 $BiFeO_3$ 纳米薄膜的微结构与铁电性能

韩亚洁[1,2]，钱　进[1,2]，王建荣[2]，林秀娟[1]，杨长红[1]，黄世峰[1]

(1. 济南大学，山东省建筑材料制备与测试技术重点实验室，济南 250022；
2. 济南大学，材料科学与工程学院，济南 250022)

摘　要：采用化学溶液法结合层层旋涂退火工艺，在掺氟氧化锡导电玻璃基片上制备了 $BiFe_{0.95}Mn_{0.05}O_3$ 和 $Bi_{0.9}Nd_{0.1}FeO_3$ 纳米晶铁电薄膜，并分析比较了其微结构和铁电性能。结果表明：2 组分样品均为单相多晶钙钛矿结构，晶粒细小均匀，表面平整，结构致密。两薄膜均获得了饱和电滞回线，且 $BiFe_{0.95}Mn_{0.05}O_3$ 薄膜具有向上的择优取向极化和更优异的铁电性能，其剩余极化强度(P_r)达 60 μC·cm^{-2}，在 1~50 kHz 频率范围与 25~200 ℃温度区间内铁电极化响应稳定，保持时间长达 1×10^3 s 工作与反复极化翻转高达 1×10^9 次表现出优异的电荷保持力和抗疲劳稳定性。

关键词：薄膜；铁酸铋；离子掺杂；微结构；铁电性
中图分类号：TB34　　**文献标志码**：A　　**文章编号**：0454–5648(2021)03–0511–08
网络出版时间：2021–01–21



Structure and Ferroelectric Properties of $BiFeO_3$ Nano-Crystalline Film Substituted at *A*/*B* Site

HAN Yajie[1,2], *QIAN Jin*[1,2], *WANG Jianrong*[2], *LIN Xiujuan*[1], *YANG Changhong*[1], *HUANG Shifeng*[1]
(1. Shandong Provincial Key Laboratory of Preparation and Measurement of Building Materials, University of Jinan, Jinan 250022, China; 2. School of Materials Science and Engineering, University of Jinan, Jinan 250022, China)

Abstract: The nano-crystalline ferroelectric films composed of $BiFe_{0.95}Mn_{0.05}O_3$ and $Bi_{0.9}Nd_{0.1}FeO_3$ were fabricated on the fluorine-doped tin oxide/glass substrates via the simple and cost-effective chemical solution deposition method combined with spin-coating and the subsequent layer-by-layer annealing technique. Microstructures and ferroelectric properties of the samples were investigated. Results show that either $BiFe_{0.95}Mn_{0.05}O_3$ or $Bi_{0.9}Nd_{0.1}FeO_3$ film has a single polycrystalline perovskite phase structure with fine and homogeneous grains and smooth surface in addition to a compact and dense structure. Both film samples exhibited well-saturated polarization-electric field hysteresis loops. Especially, the $BiFe_{0.95}Mn_{0.05}O_3$ film showed more preferential upward polarization orientation and superior ferroelectric properties than the $Bi_{0.9}Nd_{0.1}FeO_3$ film, which was reflected by a high remanent polarization (P_r) of 60 μC·cm^{-2} and stable ferroelectric responses to frequency and temperature in the ranges of 1 to 50 kHz and 25 to 200 ℃ in addition to retention capability of 1×10^3 seconds and fatigue endurance over 1×10^9 cycles.

Keywords: thin film; bismuth ferrite; ion doping; microstructure; ferroelectric property

1　Introduction

Non-volatile data-storage devices, represented by phase-change, resistive, and ferroelectric random access memories (PCRAM, RRAM, and FeRAM) respectively, have been considered as one of the core component in an integrated computer circuit[1−3]. Particularly, the FeRAM based on the electrical polarization of the dipoles in ferroelectrics shares the advantages of fast and low-power read/write operations

收稿日期：2020–07–21。　修订日期：2020–08–27。
基金项目：国家自然科学基金面上项目(51972144，51632003)；国家自然科学基金联合基金项目(U1806221)；山东省重点研发计划(2019GGX102015)；泰山学者攀登计划；济南市顶尖人才“一事一议”项目；济南市“高校 20 条”项目(2019GXRC017)。
第一作者：韩亚洁(1995—)，女，硕士研究生。
通信作者：杨长红(1977—)，女，博士，教授。

Received date: 2020–07–21.　**Revised date:** 2020–08–27.
First author: HAN Yajie (1995–), female, Master.
E-mail: han_yaj@163.com
Corresponding author: YANG Changhong (1977–), female, Ph.D., Professor.
E-mail: mse_yangch@ujn.edu.cn

and large read/write cycle endurance in addition to high densities and has attracted a lot of attention for use in the realm of non-volatile digital information[4–8]. Accordingly, as a basic element of FeRAM, the high-performance ferroelectric material has gradually become the research focus of the functional electronics field.

Being different from the commercially available Pb-containing Pb(Zr, Ti)O_3 (PZT)-based ferroelectrics[9–10], perovskite bismuth ferrite ($BiFeO_3$, BFO) possesses the salient advantages of being lead-free and having ultra-high Curie temperatures (T_C–830 ℃) and ultra-large theoretical remanent polarizations (P_r–100 μC·cm^{-2}) at room temperature, which shows a great potential for outperforming the numerous ferroelectric material systems for applications[11–14]. However, the severe leakage problem in pure BFO film limits its intrinsic material properties, including electrical polarization and ferroelectric reliability, such as retention and fatigue, thus hindering future practical applications. Hence, resolution of the leakage issue has been the steady motivation of the studies addressing BFO-based films before the realization of practical devices. Among the extensive methods toward improving the electrical properties of BFO, doping ions at *A*(Bi)/*B*(Fe) sites has been proven to be an effective and simple way to improving their properties. For example, Kawae et al. found that 3% (mole fraction) Mn and 2% (mole fraction) Ti co-modified BFO film prepared by pulsed laser deposition exhibited well-saturated polarization-electric field (*P*–*E*) hysteresis loops with a large remanent polarization (P_r–75 μC·cm^{-2})[15]. Using a simple and cost-effective chemical solution deposition (CSD) method, Hu et al. reported that the BFO film co-doped with 1% (mole fraction) Ti and 1% (mole fraction) Zn at Fe sites presented good charge-retaining capability and strong fatigue resistance[16]. They also found that the leakage current density before breakdown of BFO film could be reduced by about two orders of magnitude by doping with lanthanide (Gd, 5% in mole fraction) at the Bi site[17]. Also, according to Pattanayak's report, lanthanide substitution with 5% to 15% Nd in BFO ceramics counterpart exhibited relatively low conductivity and enhanced saturated polarization[18]. Inspired by the previous studies and based on our experimental experience[19], we expect to adopt the ion doping strategy combined with the simple film deposition method of CSD to obtain a high-performance BFO-based film.

In this study, we focused on the film system composed of $BiFe_{0.95}Mn_{0.05}O_3$ (BFMO) and $Bi_{0.9}Nd_{0.1}FeO_3$ (BNFO). Especially, the BFMO film exhibited large remanent polarization with P_r of 60 μC·cm^{-2} and preferential upward polarization compared to the BNFO film. The polarization information showed good frequency stability from 1 to 50 kHz and thermal stability in the range from 25 to 200 ℃, in addition to excellent reliable long-lifetime operation with retention capability of 1×10^3 s and fatigue resistance over 1×10^9 cycles.

2 Experimental

The phase-pure BFMO and BNFO films with thicknesses in the nanoscale range were grown using a CSD method combined with spin-coating technique on fluorine-doped tin oxide (FTO)/glass substrates. An un-doped BFO film was prepared under the same processing conditions for comparison (control). Stoichiometric $Bi(NO_3)_3\cdot5H_2O$, $Fe(NO_3)_3\cdot9H_2O$ and $(CH_3COO)_2Mn\cdot4H_2O$ served as raw materials, which were dissolved in ethylene glycol and acetic acid with magnetic stirring at room temperature. Here, 5% (mole fraction) excess bismuth (Bi) was added to compensate for the Bi volatilization during thermal treatment. With moderate amount of the stabilizing agent of acetylacetone being dropped into the solution, the final BFMO solution with a concentration of 0.3 mol/L was obtained. Keeping other processing parameters constant, the precursor solutions for BNFO and pure BFO were prepared by replacing the Mn salt with $Nd(NO_3)_3\cdot6H_2O$ and removing the doped Mn element, respectively. For nano-crystalline film fabrication, each solution was spin-coated onto the clean (FTO)/glass substrates at a speed of 3 000 r/min for 30 s followed by a pyrolysis process at 300 ℃ for 2 min on a hot plate and an annealing process at 500 ℃ for 8 min in a rapid thermal processor. The spin coating and thermal treatment steps above were repeated several times until the desired thickness of each film was achieved.

The crystal phase structures of the films were identified using Cu Kα radiation with a Bruker D8 X-ray diffractometer (XRD). Surface morphologies and cross-sectional microstructures were detected using an atomic force microscope (AFM, Bruker dimension icon) and a field-emission scanning electron microscope (FESEM, Hitachi S–4200), respectively. The piezoelectric phase image was obtained through a piezoresponse force microscope (PFM) mode using the aforementioned AFM. A standard ferroelectric tester (Precision Pro. Radiant Technologies) was employed to evaluate the ferroelectric and insulating properties in addition to long lifetime duration, for example, retention and fatigue characteristics. An ultraviolet photoelectron spectroscopy (UPS, PHI5000 VersaProbe III) test was conducted to measure the work function of the sample. The operating temperature was controlled with a cooling-heating stage (RTL550–DJ).

3 Results and discussion

The crystal structures of the BFMO and BNFO films were investigated by XRD in the 2θ range of 20° to 60° as shown in Fig. 1. An XRD pattern of FTO substrate was also included in the figure to distinguish the diffraction peaks. Note that the BFMO and BNFO films demonstrated similar perovskite structures with the detectable peaks matching well with the rhombohedral *R*3*c* structure. No indication of secondary phase could be noted. The BFMO sample is found to be typically polycrystalline with strong (012) and (110) peaks. In comparison, an oriented diffraction peak of (012) with relatively weaker (110) was obtained in BNFO sample. The good crystallization characteristic may largely benefit from the facilitating impact of the oxide substrate on the nucleation and grain growth in films. The XRD results reveal a component feasibility of moderate Mn or Nd substitution in the BFO film.

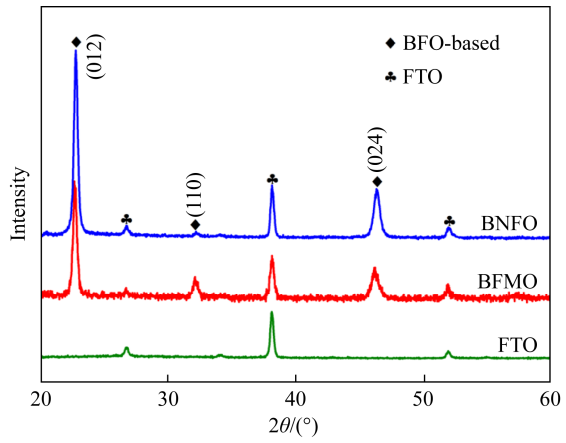
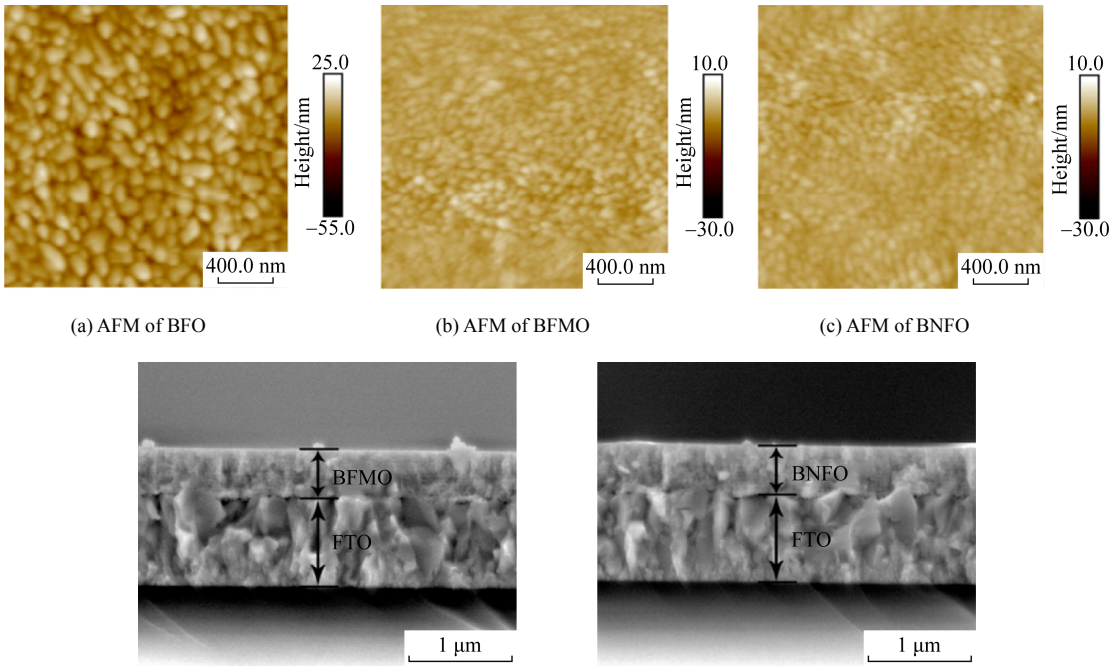


Fig. 1　X-ray diffraction patterns of the fluorine-doped tin oxide (FTO) substrate, $BiFe_{0.95}Mn_{0.05}O_3$ (BFMO), and $Bi_{0.9}Nd_{0.1}FeO_3$ (BNFO) films

The surface morphologies of the film samples were detected by scanning arbitrary areas of 2 μm×2 μm with an AFM probe. Taking the pure BFO [Fig. 2(a)] for comparison, it can be seen that both BFMO and BNFO films are well crystallized with fine and homogeneous grains as shown in Figs. 2(b) and 2(c), respectively. The grain sizes of either the BFMO or BNFO sample are much smaller than those in the pure BFO film. This finding can be understood from the point that the chemical valence fluctuation of Fe ions and the volatilization of Bi bring oxygen vacancies ($V_O^{\cdot\cdot}$) in BFO as described by the equations, $2Fe_{Fe}^{\times} + O_O^{\times} \rightarrow 2Fe_{Fe}^{'} + V_O^{\cdot\cdot} + \frac{1}{2}O_2$ and $2Bi_{Bi}^{\times} + 3O_O^{\times} \rightarrow 2V_{Bi}^{'''} + 3V_O^{\cdot\cdot} + Bi_2O_3$. The hetero-valent Mn doping at the Fe site and iso-valent Nd substitution at the Bi site contribute to the reduction of movable $V_O^{\cdot\cdot}$ in BFO by filling up the $V_O^{\cdot\cdot}$ according to the reactions of $Mn^{2+} + V_{Fe}^{'''} \rightarrow Mn_{Fe}^{'}$ and $2Mn_{Fe}^{'} + V_O^{\cdot\cdot} + \frac{1}{2}O_2 \rightarrow 2Mn_{Fe}^{\times} + O_O^{\times}$ and by suppressing the volatilization of Bi with $Nd^{3+} + V_{Bi}^{'''} \rightarrow Nd_{Bi}^{\times}$ [20–21]. Since the vacancy diffusion mechanism is vital for ion diffusion during the crystallization of crystals, the reduced $V_O^{\cdot\cdot}$ affects ion diffusion, thus affecting the transfer of mass and energy between reactants during the crystallization process and limiting the grain growth for the doped films[22–23]. Note that all samples were relatively dense and smooth with no obvious cracks or pinholes scattered on the surfaces. Derived from the AFM images, the root mean square roughness (R_{rms}) of BFO was 5.04 nm, while the R_{rms} values of BFMO and BNFO were only 1.130 and 1.06 nm, respectively. The smooth surfaces resulting from the highly-uniform grain sizes would be favorable for the micro-devices in integrated circuits. Figs. 2(d) and 2(e) present the cross-sectional FESEM images of the BFMO and BNFO film samples, respectively. The microstructures of both films are relatively compact without obvious pinholes. The clear film/substrate interfaces without substantial cation inter-diffusions across them can be found in the BFMO and BNFO samples, indicating good heterostructure qualities. Each sample has a thickness of about 400 nm.

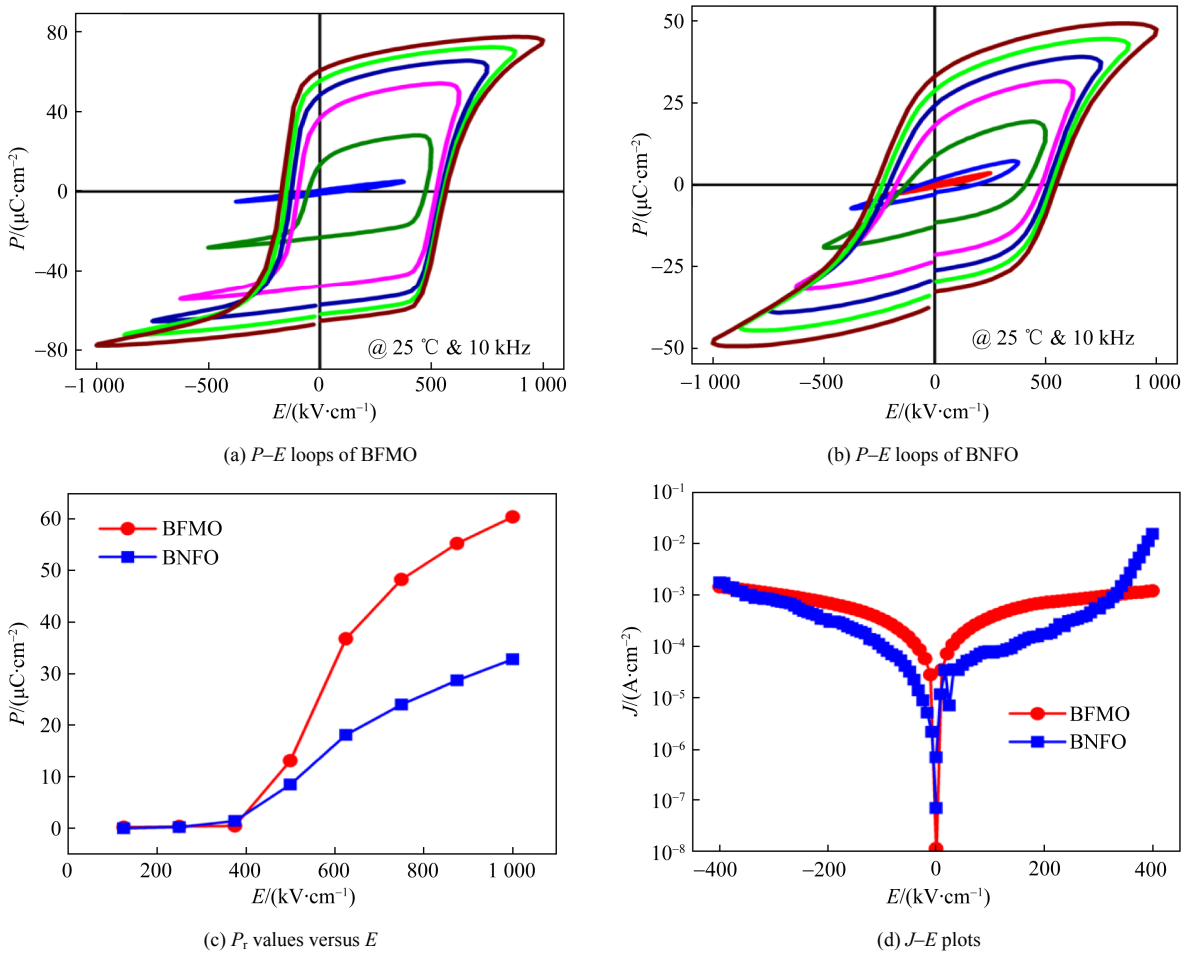
The macroscopic ferroelectric properties of the films were measured at ambient temperature. Figs. 3(a) and 3(b) show the *P*–*E* hysteresis loops of BFMO and BNFO in which a high frequency of 10 kHz was applied. Positive shifts along horizontal axis, *i.e.*, asymmetrical coercive field (E_c), could be observed apparently from all the *P*–*E* loops, especially for the BFMO film, indicating the preferential upward polarization state in the films. With the electric field increasing from 125 kV·cm^{-1} to the maximum *E* that the film could withstand, the *P*–*E* loops tended to saturate gradually. As the electric field is elevated up to 1 000 kV·cm^{-1}, the saturated polarization (P_s) for BFMO and BNFO films were 76 and 48 μC·cm^{-2}, respectively, while the P_r of BFMO and BNFO samples were 60 and 33 μC·cm^{-2}, respectively [also in Fig. 3(c)]. In comparison with the ever-reported pure BFO films[17, 24], the electrical polarizations for the doped films in this work were dramatically improved, which could be attributed to the effectively suppressed free $V_O^{\cdot\cdot}$ via Mn substitution for Fe in BFMO and Nd doping at Bi for BNFO. Particularly, such a high P_r of 60 μC·cm^{-2} obtained from the BFMO film was even comparable to that obtained in the single crystalline



(a) AFM of BFO (b) AFM of BFMO (c) AFM of BNFO

(d) FESEM of BFMO (e) FESEM of BNFO

Fig. 2 Atomic force microscopy (AFM) surface morphologies of pure BFO, BFMO, and BNFO, cross-sectional field-emission scanning electron microscopy (FESEM) images of BFMO and BNFO films



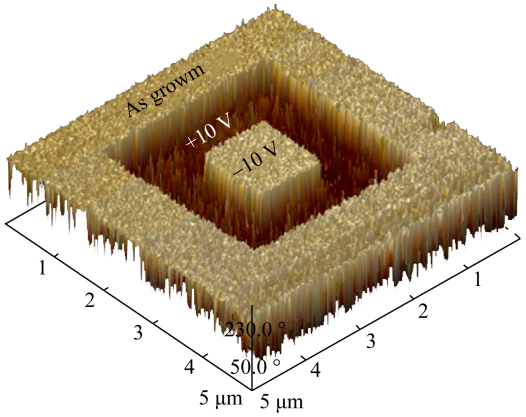
(a) *P*–*E* loops of BFMO (b) *P*–*E* loops of BNFO

(c) P_r values versus *E* (d) *J*–*E* plots

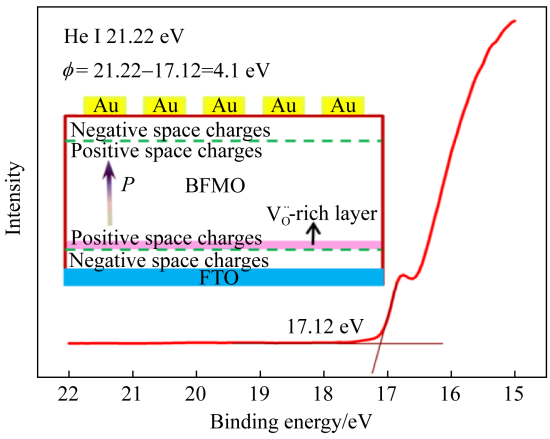
Fig. 3 Room-temperature polarization-electric field (*P*–*E*) hysteresis loops, P_r values and leakage current densities as functions of electric fields (*J*–*E*) of BFMO and BNFO films

Ti-rich PZT film[3]. However, unfortunately, as a response to the space charge effect existed in film, the *P*–*E* loop of BNFO film takes on some rounding shapes at high *E* regions, which is consistent with the relatively severe leakage current in film at high *E* as shown in Fig. 3(d). Such a phenomenon frequently occurs in the perovskite ferroelectric materials[25–26]. Considering that the BFMO sample shows a more preferable ferroelectric polarization and lower leakage at high *E* than BNFO, further investigations into the ferroelectric properties of BFMO were carried out in the following sections.

The microscopic ferroelectric polarization switching behavior of BFMO film was investigated by piezoelectric force microscopy (PFM). After selecting an area of 5 μm×5 μm, poling treatments were conducted by applying a direct current (DC) bias of +10 V with a conductive tip in the central 3 μm×3 μm first and then another DC tip bias of −10 V in the central square region of 1 μm×1 μm. A box-in-box domain configuration was then read out by scanning the whole 5 μm×5 μm region as shown in Fig. 4(a). Note that bright and dark contrasts corresponding to the up and down polarization are clear in the regions with reverse voltages. The switchable polarization confirms the ferroelectric nature in the film[3]. Also, the contrast in the as-grown region was similar to that in the negatively poled area, reflecting a preferential upward polarization state that consistent with the shifts of *P*–*E* loops [Fig. 3(a)]. Such a phenomenon mainly resulted from the internal electric field formed in film, which was a result of the combination of the movable ions or space charges, such as $V_O^{\cdot\cdot}$, which accumulated at the film/electrode interfaces and the small difference in the work functions (ϕ) between the BFMO film [ϕ_{BFMO}=4.1 eV in Fig. 4(b)] and the bottom (ϕ_{FTO}= 5.0 eV) and top (ϕ_{Au}=5.1 eV) electrodes[27–29]. The inset of Fig. 4(b) schematically illustrates the formation mechanism of the preferential upward polarization of the BFMO film in which the colored arrow stands for the polarization direction of BFMO, and the green dashed lines denote the film/electrode interfaces of BFMO/Au and BFMO/FTO. Especially, because of the spin coating and subsequent layer-by-layer annealing technique adopted in this work, the film layers near the bottom electrode experienced more high-temperature annealing treatments. This type of treatment caused $V_O^{\cdot\cdot}$ to gradually accumulate near the bottom layer to generate a $V_O^{\cdot\cdot}$-rich defect layer near the film/bottom electrode thus forming an upward local electric field to contribute to the upward polarization predominantly. Interestingly, the preferential polarization orientation formed in the as-grown BFMO film without any external electric field excitation also makes it appealing for piezoelectric device applications because it offers the possibility of omitting poling process and reducing production costs.



(a) PFM image



The inset shows a schematic illustration of preferential upward polarization for BFMO film in which the colored arrow stands for the polarization direction, and the dashed lines denote the film/electrode interfaces.

(b) UPS spectrum

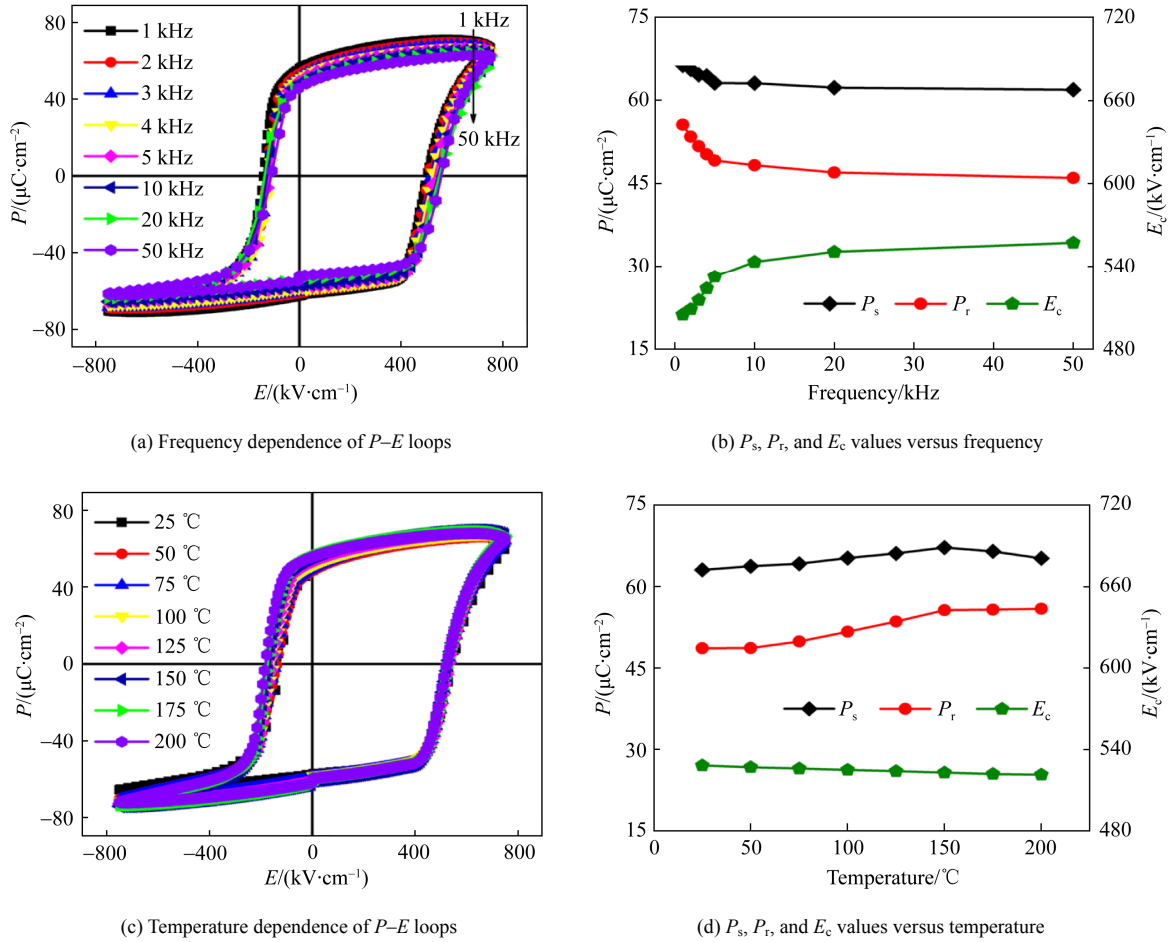
Fig. 4　3D view of out-of-plane piezoelectric force microscopy (PFM) phase image for BFMO film in which the regions of 3 μm×3 μm and 1 μm×1 μm were written on the sample by applying the DC tip bias of +10 V and –10 V, respectively, and an ultraviolet photon spectroscopy (UPS) spectrum for BFMO with He I as light source

Stable ferroelectric responses to frequencies over a wide operating range are essential for the ferroelectric applications in non-volatile memories. Fig. 5(a) shows the *P*–*E* loops ranging from 1 kHz to 50 kHz at 750 kV·cm^{-1} and room temperature of the BFMO film. Note that all the loops display some dependence on the measuring frequency. Extracting the key parameters from *P*–*E* data, the corresponding values of P_s, P_r, and

E_c versus frequency are shown in Fig. 5(b). As the frequency increased from 1 to 50 kHz, the P_s and P_r values decreased from 66 to 62 μC·cm^{-2} and from 55 to 46 μC·cm^{-2}, respectively, whereas E_c increases from 505 to 557 kV·cm^{-1}. The results reveal a weak dependence of polarization behavior on measuring frequency, meaning a good frequency stability of BFMO, which benefits from the nonlinear dielectric effects of ferroelectrics and fast domain switching in addition to low leakage in film[13].

Thermal stability is a significant parameter for ferroelectric devices to evaluate their working feasibility under harsh environmental conditions. Fig. 5(c) shows the temperature dependence of *P*–*E* loops measured with 750 kV·cm^{-1} at 10 kHz for BFMO films in the range of 25–200 ℃. For clarity, Fig. 5(d) shows the changes in P_s, P_r, and E_c values as functions of temperature. Note that the fluctuations of P_s, P_r, and E_c over the entire temperature range were within 7%, 13%, and 2%, respectively, demonstrating a thermally stable ferroelectric property, which is even on a par with that obtained in the flexible (Mn,Ti)-codoped BFO film [13].

Long-term working stability is indispensable for the practical applications of memory devices. Hence, we now turn our attention to the retention and fatigue characteristics of BFMO films. Fig. 6(a) shows the normalized pulsed remanent polarization (Δ*P*, defined as $P^*–P^{\wedge}$ in which the P^* represents switched polarization and $P^{\wedge}$ stands for non-switched polarization) as a function of retention time for the BFMO film, which was recorded by the write and read electric fields of 750 kV·cm^{-1} with the pulse width of 100 μs. Note that the BFMO memory component could retain more than 91% of its initial polarization as the retention time is up to 1×10^3 s, demonstrating an excellent charge-retaining ability. A fatigue test at 750 kV·cm^{-1} and 1 MHz demonstrated that the polarization information did not show any loss even after 1×10^9 switching cycles as shown in Figs. 6(b) and 6(c). To the best of our knowledge, the diffusion of $V_O^{\cdot\cdot}$ and the electronic charge trapping at domain wall mainly account for the fatigue behavior during the repeated switching[24]. Thus, we hold the opinion that the satisfactory fatigue endurance in BFMO is mainly rooted in the decline of movable charge carriers with Mn doping.



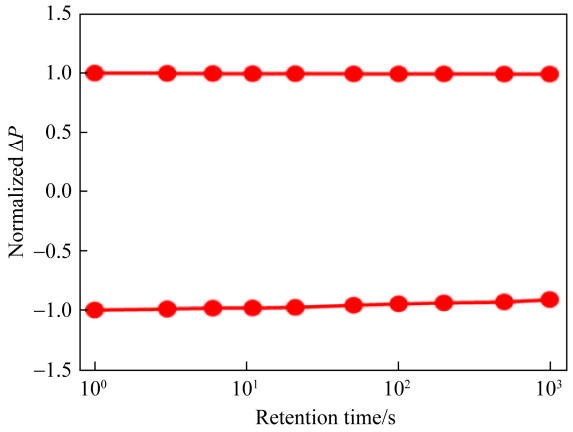
(a) Frequency dependence of *P*–*E* loops

(b) P_s, P_r, and E_c values versus frequency

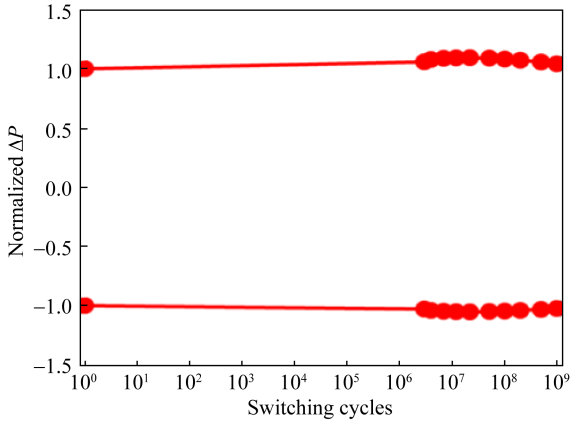
(c) Temperature dependence of *P*–*E* loops

(d) P_s, P_r, and E_c values versus temperature

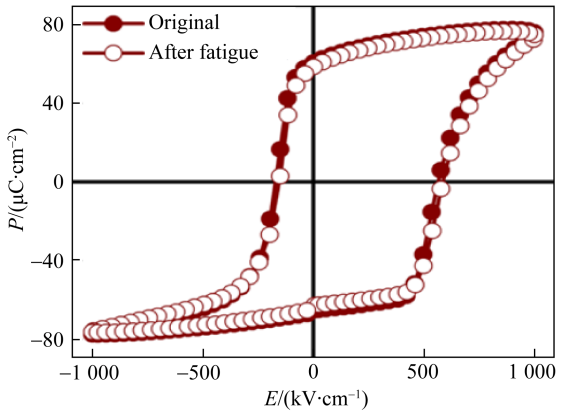
Fig. 5 *P*–*E* loops, and corresponding P_s, P_r, and E_c values for the BFMO film as functions of frequency and temperature



(a) Retention



(b) Fatigue



(c) *P*–*E* loops

Fig. 6　Normalized pulsed remanent polarization as functions of retention time and fatigue cycles, and the corresponding *P*–*E* loops before and after 1×10^9 polarization switching for BFMO film

4　Conclusions

In summary, we report on successful fabrications of BFMO and BNFO films on the FTO/glass substrates using CSD. Microstructure characterizations show that the BFMO and BNFO films are crystallized into single polycrystalline perovskite phases with homogeneous and dense structures in addition to smooth surfaces. *P*–*E* tests show that both samples exhibit well-saturated hysteresis loops. Compared with BNFO, the BFMO film possesses optimal ferroelectric properties with a high P_r of 60 μC·cm^{-2} and stable frequency response in the range of 1 to 50 kHz and thermal stability of 25 ℃ to 200 ℃ in addition to a preferential polarization orientation. Besides, satisfactory long-term ferroelectric reliabilities could be achieved in the BFMO film, which is represented by the charge-retaining ability of 1×10^3 s and fatigue-free characteristic over 1×10^9 cycles. All the results obtained in BFMO render it appealing for practical applications in the e-markets concerning ferroelectric and piezoelectric devices.

References:

[1] DING K Y, WANG J J, ZHOU Y X, et al. Phase-change heterostructure enables ultralow noise and drift for memory operation[J]. Science, 2019, 366(6462): 210–215.

[2] YANG Y X, YUAN G L, YAN Z B, et al. Flexible, semitransparent, and inorganic resistive memory based on $BaTi_{0.95}Co_{0.05}O_3$ film[J]. Adv Mater, 2017, 29(26): 1700425.

[3] JIANG J, BITLA Y, HUANG C W, et al. Flexible ferroelectric element based on van der waals heteroepitaxy[J]. Sci Adv, 2017, 3(6): e1700121.

[4] SCOTT J F. Data storage multiferroic memories[J]. Nat Mater, 2007, 6(4): 256–257.

[5] GARCIA V, BIBES M. Ferroelectric tunnel junctions for information storage and processing[J]. Nat Commun, 2014, 5: 4289.

[6] LEE D, YANG S M, KIM T H, et al. Multilevel data storage memory using deterministic polarization control[J]. Adv Mater, 2012, 24(3): 402–406.

[7] YANG C H, HAN Y J, QIAN J, et al. Flexible, temperature-stable, and fatigue-endurable $PbZr_{0.52}Ti_{0.48}O_3$ ferroelectric film for nonvolatile memory[J]. Adv Electron Mater, 2019, 5(10): 1900443.

[8] OWCZAREK M, HUJSAK K A, FERRIS D P, et al. Flexible ferroelectric organic crystals[J]. Nat Commun, 2016, 7: 13108.

[9] GHONEIM M T, ZIDAN M A, ALNASSAR M Y, et al. Thin PZT-based ferroelectric capacitors on flexible silicon for nonvolatile memory applications[J]. Adv Electron Mater, 2015, 1(6): 1500045.

[10] BAKAUL S R, SERRAO C R, LEE O, et al. High speed epitaxial perovskite memory on flexible substrates[J]. Adv Mater, 2017, 29(11): 1605699.

[11] WANG J, NEATON J B, ZHENG H, et al. Epitaxial $BiFeO_3$ multiferroic thin film heterostructures[J]. Science, 2003, 299(5613): 1719–1722.

[12] CATALAN G, SCOTT J F. Physics and applications of bismuth ferrite[J]. Adv Mater, 2009, 21(24): 2463–2485.

[13] YANG C H, HAN Y J, QIAN J, et al. Flexible, temperature-resistant, and fatigue-free ferroelectric memory based on $Bi(Fe_{0.93}Mn_{0.05}Ti_{0.02})O_3$ thin film[J]. ACS Appl Mater Interfaces, 2019, 11(13): 12647–12655.

[14] YANG C H, QIAN J, LV P P, et al. Flexible lead-free BFO-based dielectric capacitor with large energy density, superior thermal stability, and reliable bending endurance[J]. J Materiomics, 2020, 6(1):

200–208.

[15] KAWAE T, TERAUCHI Y, TSUDA H, et al. Improved leakage and ferroelectric properties of Mn and Ti codoped $BiFeO_3$ thin films[J]. Appl Phys Lett, 2009, 94(11): 112904.

[16] HU G D, FAN S H, YANG C H, et al. Low leakage current and enhanced ferroelectric properties of Ti and Zn codoped $BiFeO_3$ thin film[J]. Appl Phys Lett, 2008, 92(19): 192905.

[17] HU G D, CHENG X, WU W B, et al. Effects of Gd substitution on structure and ferroelectric properties of $BiFeO_3$ thin films prepared using metal organic decomposition[J]. Appl Phys Lett, 2007, 91(23): 232909.

[18] PATTANAYAK S, CHOUDHARY R N P. Synthesis, electrical and magnetic characteristics of Nd-modified $BiFeO_3$[J]. Ceram Int, 2015, 41(8): 9403–9410.

[19] WEN Z, HU G D, FAN S H, et al. Effects of annealing process and Mn substitution on structure and ferroelectric properties of $BiFeO_3$ films[J]. Thin Solid Films, 2009, 517(16): 4497–4501.

[20] PAN H, ZENG Y, SHEN Y, et al. $BiFeO_3$–$SrTiO_3$ thin film as a new lead-free relaxor ferroelectric capacitor with ultrahigh energy storage performance[J]. J Mater Chem A, 2017, 5(12): 5920–5926.

[21] JIANG B, LI X L, ZHANG H Y, et al. Large and stable piezoelectric response in $Bi_{0.97}Nd_{0.03}FeO_3$ thin film[J]. Appl Phys Lett, 2012, 100(17): 172904.

[22] LIU H Y, PU Y P, SHI X, et al. Dielectric and ferroelectric properties of $BiFeO_3$ ceramics sintered in different atmospheres[J]. Ceram Int, 2013, 39(S1): S217–S220.

[23] SAKAMOTO W, IWATA A, MORIYA M, et al. Electrical and magnetic properties of Mn-doped $0.7BiFeO_3$–$0.3PbTiO_3$ thin films prepared under various heating atmospheres[J]. Mater Chem Phys, 2009, 116(2/3): 536–541.

[24] CHENG Z X, WANG X L, DOU S X, et al. Improved ferroelectric properties in multiferroic $BiFeO_3$ thin films through La and Nb codoping[J]. Phys Rev B, 2008, 77(9): 092101.

[25] QI X D, DHO J, TOMOV R, et al. Greatly reduced leakage current and conduction mechanism in aliovalent-ion-doped $BiFeO_3$[J]. Appl Phys Lett, 2005, 86(6): 062903.

[26] WALENZA–SLABE J, GIBBONS B J. Effect of annealing atmosphere pO_2 on leakage current in $80(Bi_{0.5}Na_{0.5})TiO_3$–$20(Bi_{0.5}K_{0.5})TiO_3$ piezoelectric thin films[J]. Appl Phys Lett, 2017, 110(16): 162904.

[27] MIAO P X, ZHAO Y G, LUO N N, et al. Ferroelectricity and self-polarization in ultrathin relaxor ferroelectric films[J]. SCI REP–UK, 2016, 6: 19965.

[28] SIMÕES A Z, RAMÍREZ M A, RICCARDI C S, et al. Synthesis and electrical characterization of $CaBi_2Nb_2O_9$ thin films deposited on $Pt/Ti/SiO_2/Si$ substrates by polymeric precursor method[J]. Mater Chem Phys, 2006, 98(2/3): 203–206.

[29] LIN Q R, DING R, LI Q, et al. Large piezoelectricity and ferroelectricity in Mn-doped $(Bi_{0.5}Na_{0.5})TiO_3$–$BaTiO_3$ thin film prepared by pulsed laser deposition[J]. J Am Ceram Soc, 2016, 99(7): 2347–2353.